E-Journal of Advanced Maintenance Vol.3 (2011) 54-77
Japan Society of Maintenology

Computational Challenges in Numerical Simulations of ISI of Ferritic Steam Generator Tubes in Fast Breeder Reactors using Eddy Currents and Multi-frequency Algorithms

Ovidiu MIHALACHE , Toshihiko YAMAGUCHI, Masashi UEDA

Japan Atomic Energy Agency, Fast Breeder Reactor Plant Engineering Research Center, Operation and Maintenance Technology Development Group, 1 Shiraki, Tsuruga-shi, Fukui-ken, 919-1279, Japan

ABSTRACT

In the present paper are addressed the challenges of three dimensional (3D) simulations of ISI of ferritic SG tubes in FBR using ECT. The performance of 3D computation is analyzed for a specific FBR case, where there is a simple or complex tube support plate (SP) structure with one or multiple tubes connected to it, and sodium, which generates an additional noise in the ECT signal. Signal enhancement by means of multi-frequency ECT techniques are validated through 3D simulations of both signals and noise due to sodium forms around SG tube or SP.

KEYWORDS

eddy currents, steam generator, fast breeder reactor, sodium, in-service inspection, finite element method, multi-frequency, support plate

ARTICLE INFORMATION

Article history:
Received #12 May 2011
Accepted #21July 2011

1. Introduction

In Fast Breeder Reactors (FBR) using liquid sodium as a coolant, In-Service Inspection (ISI) of Steam Generator (SG) tubes based on Eddy Currents Testing (ECT) has to consider the electromagnetic interferences from the conductive sodium. In the heat-exchanger system of FBR, low pressure liquid sodium at high temperature (around 500 ºC) flows in the SG vessel, while high pressure steam-water runs through SG tubes. ISI for SG tubes is conducted from the inside of tubes after liquid hot sodium is drained from vessel and cooled down to room temperature. After sodium draining sodium adheres to the outer surface of SG tubes in thin non-uniform layers, which was also confirmed experimentally by authors in the past [1].

While sodium is a paramagnetic substance and can be considered to have a relative magnetic permeability close to that of the vacuum, presence of ferromagnetic impurities, could lead to variations of its relative magnetic permeability. By maintaining a high level of purity of liquid sodium and removing oxides, no variations of magnetic susceptibility with the magnetic field intensity were found [2]. However, sodium electrical conductivity (23.8×10^6 S/m) is very high, and consequently thin layers of sodium or sodium deposits add additional noise during ECT inspection. Because the distribution of sodium layers or drops on the outer SG tubes surface after each draining cannot be controlled, numerical simulations are employed to validate multi-frequency ECT algorithms and confirm reliable ISI of SG tubes.

The Japanese prototype FBR Monju SG tubes are made of both austenitic stainless steel for superheater (SH) and ferritic Chromium-Molybdenum (Cr-Mo) alloy steel for evaporator (EV). In addition to the standard ECT for austenitic stainless steel, a Remote Field Eddy Current Testing (RF-ECT) is employed for ISI of ferromagnetic Cr-Mo alloy tubes [3-7]. The SG tubes of FBR, EV and SH are bundled in a cylindrical vessel filled with sodium. Because the outer part of SG tubes is covered by sodium and not accessible, the tubes are inspected only from the tube inside for defects on both inner and outer tube surface. In spite of long size of tubes (84 m for EV and 46 m for SH), ECT probes are able to inspect all SG tubes. For ferromagnetic EV tubes, RF-ECT is able to detect both inner/outer tube defects.

In the numerical simulations of the ISI of FBR SG tubes using ECT, finite element method

(FEM) is used in order to model complex geometries including: multiple SG tubes, different sodium forms, and additional structures such as SG support plates (SP). Three-dimensional (3D) modeling and electromagnetic analysis are based on the 3D-RFECT parallel code, developed in-house for a nodal-magnetic vector implementation and FEM modeling [8].

The present paper deals with the challenges in the numerical computation of ISI of ferritic SG tubes using RF-ECT, in order to evaluate the effect of sodium structures outside SG tubes and their electromagnetic interaction with SG support plates, and by employing multi-frequency ECT.

Section 2 describes the main challenges in numerical simulation of ISI for FBR SG tubes using RF-ECT and the extension of modeling from simple two-dimensional (2D) axisymmetric geometries to realistic three-dimensional descriptions.

Section 3 introduces the application of multi-frequency RF-ECT and numerical FEM simulations in order to evaluate ECT signal resulting from accumulation of sodium on the outer SG tube surface. Numerical simulations are extended from models of a single tube with small support plate, to those with multiple tubes and a large support plate, in order to account for effects of electromagnetic shielding due to surrounding SG tubes.

2. ISI of ferritic SG tubes of FBR using RF-ECT. FEM numerical aspects

2.1. RF-ECT for FBR ferromagnetic tubes

In the ISI of SG tubes, remote field eddy current testing (RF-ECT) is a well known method used to detect both inner and outer tube defects with equal sensitivity [3]. While this techniques is mainly applicable to ferromagnetic tubes, at low inspection frequencies (lower than 1 kHz), it has also been applied to non-magnetic SG tubes made of brass and nickel-base superalloy [4]. Fig. 1 shows a typical RF-ECT system consisting of an excitation driven coil and a detection coil, usually separated by a 2~3 tube diameters distance. During ISI both coils move inside tubes along their length: excitation coils generate electromagnetic waves whose interaction with discontinuities is recorded by detection coils. Typical ECT signal from detection coils consist either in two e.m.f. signals representing the real (or resistive) component and imaginary (or inductive) component or their combined Lissajous representation. Eddy currents at low frequency are able to penetrate the ferromagnetic tubes and their propagation along the tube wall is back-penetrating in a remote area. A typical representation of the magnetic vector potential distribution, describing the electromagnetic interaction, is shown in Fig. 1 right side.

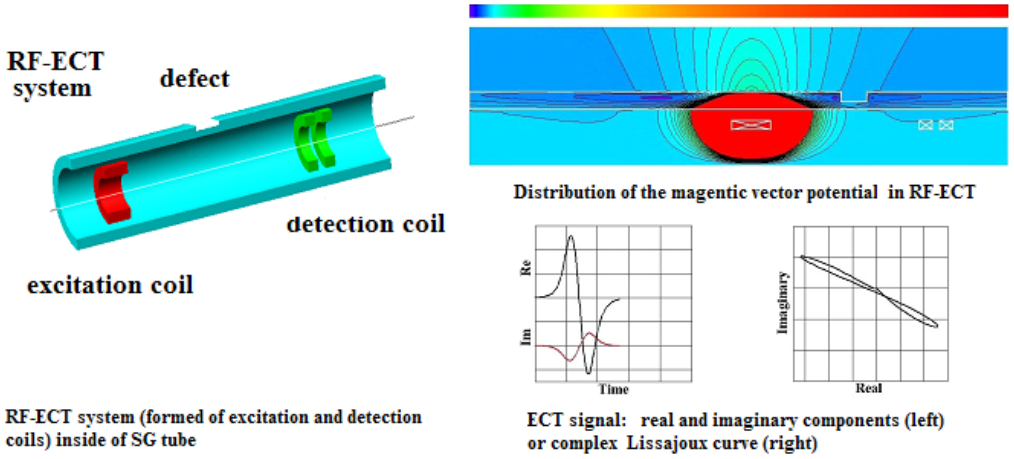

Fig. 1. RF-ECT system and Lissajous signal due to a defect in SG tube

From a numerical point of view, RF-ECT simulations require an accurate description not only of the detection and reception areas, but also of the area between both of them, which represents a great challenge in 3D. While 2-dimensional (2D) axisymmetric numerical simulations are fast and accurate, they are limited to very simple geometrical models. Previous 2D FEM simulations showed that

accuracy of the numerical simulations is strongly related to the accurate interpolation of the variation of the electromagnetic field, which decreases by more than two orders of magnitude when propagating from excitation to detection zones. 2D analyses showed that the large range of variations in RF-ECT could be well modeled in a FEM model only when coupled with 2nd order finite elements (triangles for 2D or tetrahedrons for 3D case).

In the ISI of ferromagnetic FBR SG tubes, highly electrical conductive sodium generates an additional noise in the electromagnetic signal picked-up by the detection coil. After draining the liquid sodium from the FBR SG vessel at high temperature, sodium adheres in thin layers to the outer surface of SG tubes. Experimental measurements of sodium layer thickness showed values ranging from 10μm to 50μm, while sodium drops were also formed in various location on SG tubes: next or near tube SP, under the bottom of SP, under the bottom of horizontal SG tubes [1]. Also, for outer tube defects, partial filling of defects with sodium was observed. Overall, multiple sodium draining experiences resulted in various filling factors and sodium forms distribution.

In the numerical simulations of ISI of FBR tubes using ECT, the variability of sodium forms and positions along SG tubes and structures around SG tube has to be taken into account in the most conservative case, and even if those shapes were actually not observed in the limited number of experimental measurements. ISI feasibility of FBR SG tubes using ECT should take into account accurate numerical modeling of all electromagnetic noises due to coupling of sodium with tube discontinuities, SP, or other structures around SG tubes.

The present paper applies numerical methods based on FEM using the previously developed 3D-RFECT code to model electromagnetic effect of sodium, and estimates the maximum noise arising from sodium deposition. Modeling focuses on the multiple interactions among sodium, tube, and tube support plate, because those signals could mask outer SG tube defects.

Two geometries are taken into account in 3D: the first one consists in a single SG tube with a small SP attached to it, while the second model has nine SG tubes connected to a large SP. The single tube model is representative of a small scale mockup, while the multiple tubes model is closer to the actual FBR SG configuration. The combination of these two models should therefore allow filling the uncertainty gap between ISI results in the experimental mockup and those in the actual reactor.

Fig. 2 shows the geometry of the single SG tube model with a small SP. The SP plate has mainly two legs and 2 inner rings, as detailed in Fig. 2 (left). Each leg is 20 mm wide and is positioned 60 mm apart from the other. The inner rings, made of austenitic stainless steel, fit together under the SP first leg to fix the SG tube to the SP. The second SP leg is not connected to the SG tube, and there is a 2-3 mm air gap between them.

Fig. 3 shows the geometry of nine SG tubes connected to a large SP, whose properties are similar to that of the simpler model in Fig. 2.

In both models, outer tube defects are located in either the area "A" or "B" as shown on Fig. 2, i.e. on the tube portion under both SP legs. A defect can appear in position "A" due thermal expansion of tube and fretting-wear mechanism. While there is no physical mechanism which could lead to a defect in position "B", in simulations was also added this position in order to compare the results. After draining sodium, in the most conservative approximation, sodium is filling 100% of the gap between SP and tube, around the ring and 1st leg of SP. Numerical simulations investigate separately the effect of either upper or lower filling, named “sodium (up)” and “sodium (down)” respectively, as well as their combined effect. In the "sodium (up)" or "sodium (down)" configuration sodium is filling only the upper-half or the down-half of the air-gap volume between SP and tube. The volume of sodium form filling 100% the gap between 2nd leg of SP and tube is also included in simulations as a representative of the worst case scenario conditions. Simulations investigate sodium noise on each configuration separately, as well as the noise from a combination of all cases, through different ECT algorithms based on the multi-frequency technique.

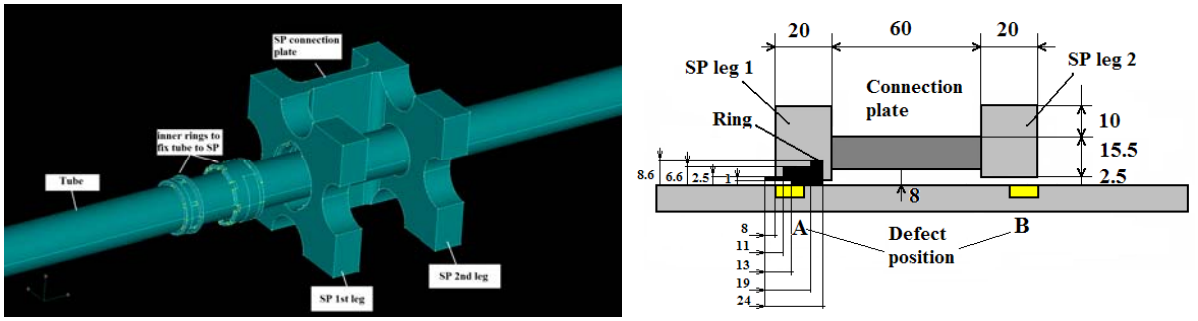

Fig. 2. Geometry (left picture) and schematics (right picture) of small SP with a single SG tube in an axisymmetric view

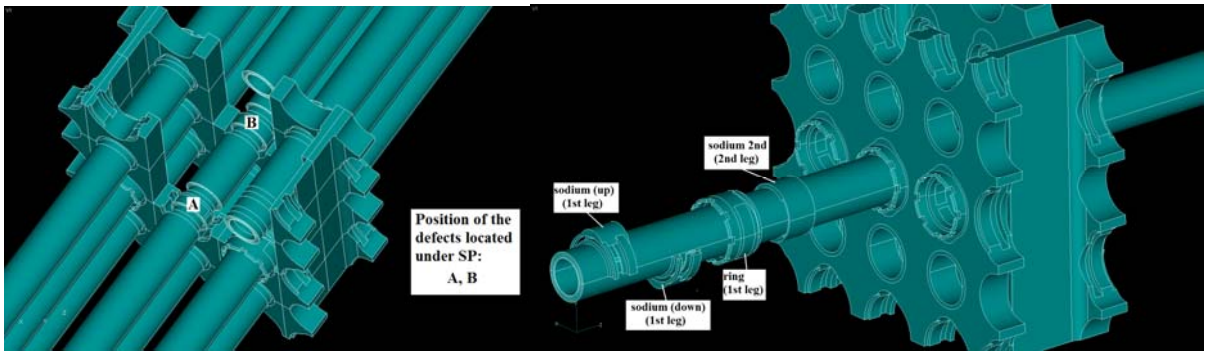

a) b)

Fig. 3. a) Geometry of large SP with nine SG tubes and defects located under SP; b) Illustration of upper half and lower half of sodium that fills completely the air gap near the ring between tube and SP

2.2. FEM model and numerical aspects of ISI using ECT: computational challenges

In FEM, the volume of interest, including SP, multiple SG tubes and sodium structures is meshed using 2nd order tetrahedrons to proper simulate the range of field variations resulting from RF-ECT (Fig. 4). The volume boundary is set far enough from both tubes and SP (300 mm and 500 mm in axial and radial directions, respectively) in order to minimize the boundary effect, based on approximations from numerical 2D axisymmetric FEM simulations [9]. The length of simulated SG tube in Z-direction is 600 mm with SP located in the central part of tube. The SP signal is computed by starting the simulations from a configuration where the center of detection coil system is 100 mm far from the edge of the 1st SP leg. There is a 50 mm pitch between outer surface of multiple SG tubes in both X and Y-direction (as in Fig. 4). The FEM mesh has at least 5 layers in the SG tubes wall to ensure accurate description of the eddy current penetration, and then gets coarser when heading towards the external boundary in order to reduce the overall number of elements, reducing both the computational burden and numerical error propagation. FEM numerical simulations of RF-ECT showed that extra care has to be paid to FEM mesh. Poor quality coarse meshes result in inaccurate simulated RF-ECT signals, while too large ones induce numerical instabilities that affect the convergence of the iterative FEM solver.

The geometrical parameters of the tubes and electromagnetic properties of all of the components (tubes, SP, detection and excitation coils) are detailed in Table 1. The inner ring connecting SG tube

to SP is not magnetic with air relative magnetic permeability and 10^6 S/m electrical conductivity. The inner ring (made of two parts as shown in Fig. 2) fit together between SP and SG tube. Their intricate shape could be easily modeled three-dimensional in FEM, and also it could be estimated the air-volume in the gap between SP, rings and SG tube. In the modeling, the air-volume was later assumed to be 100% filled with sodium, in the worst case-scenario. A simplified model of ring is shown in Fig. 2 (right).

The relative permeability of EV tube was determined from measurements of virgin curve of 2.25Cr-1Mo alloy and was determined to be close to 100 at low fields density around 50 Gauss. However, values of relative permeability close to 95 resulted from validation of simulation-experimental RF-ECT measurements conducted in-house with EV tubes with standard outer and inner grooves at various frequencies between 150 and 500 Hz.

In comparison to SG tubes, sodium is highly conductive, but in practice its relative magnetic permeability can be considered equal to 1. The electrical conductivity of solid and liquid sodium at various temperatures is listed in [2]. The excitation frequencies focus on two values, which will be later considered in the multi-frequency algorithm: 150 Hz and 450 Hz. The RF-ECT sensor has two excitation coils located before and behind detection system.

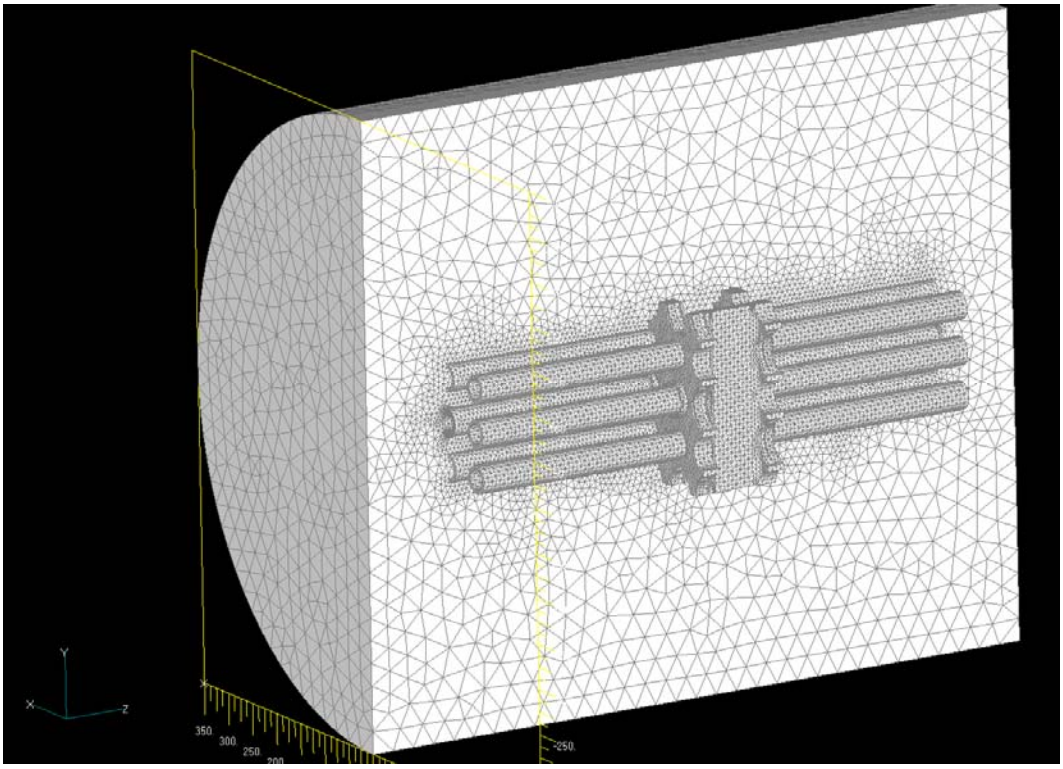

Fig. 4. FEM model for a large SP with nine SG tubes

Table 2 describes the configuration of different simulation cases that were analyzed in order to generate the electromagnetic noise from sodium when there are defects under the tube SP. The models are separated in two groups: one related to the case with a small SP and a single SG tube and the other one to the case of a large SP with nine SG tubes. Because the electromagnetic effect of sodium on the signal is not linear, several distributions of sodium and a combination of them were considered. While in experimental measurements partial filling of the gap between SP and tube and around the ring connecting SP and tube was observed, numerical simulations took into consideration the most conservative case, which is for either 50% or 100% sodium filling. The initiation of a tube outer defect under SP, can be the result of fretting-wearing mechanism due to tube thermal expansion. Again, while experimental evidence showed only small quantities of sodium accumulated in the defect area (5%~10% sodium filling), numerical simulations were concerned with the worst case scenario when sodium fills 50% or even 100% of the defect volume. For example, the situation with

sodium building right in the defect volume could be considered as a filling of the defect with sodium. From a probabilistic point of view it is expected for smaller and deeper cracks to be filled completely with sodium, while wider defects to be filled only partially, which were also observed experimentally. However, the ISI of FBR SG tubes should be based on algorithms that are validated on the most conservative cases using numerical tools, even if these cases were not directly observed in experimental measurements.

Table 1 Parameters of SG tubes, sodium and RF-ECT probe used in ISI for EV

EV tube and sodium parameters	***Value***
Inner/outer radius of SG tube	12.1mm /15.9 mm
EV tube relative magnetic permeability	95~100
EV tube electrical conductivity	$3.5x10^6$ S/m
Inner radius for OD 50%tw groove	14 mm
Length of OD 50%tw groove	10 mm
Sodium relative magnetic permeability	1
Sodium electrical conductivity	$23.8x10^6$ S/m
Parameters related to the RF-ECT probe	***Value***
Inner / outer radius of detection coil	7.75 mm / 9.75 mm
Inner / outer radius of excitation coil	7.75 mm / 9.75 mm
Current density in the excitation coil	1 A/mm^2
Number of turns in detection coil	900 turns
Excitation frequency	150 Hz, 450 Hz
Length of excitation / detection coil	15 mm / 5 mm
Distance between detection coils	3 mm
Distance between excitation-detection coil	89 mm
Signal pre-amplification	$\sim10^3$

Table 2 Description of the simulation cases for small and large model of SP

Simulation case	*Detailed description*
	1 tube - small SP model / 9 tubes - large SP model
SP	SP only
SP+defect(A)	SP and defect in position "A" under SP
SP+defect(B)	SP and defect in position "B" under SP
SP+sodium(down)	SP and sodium filling the lower-half of gap under 1st leg of SP
SP+sodium(up)	SP and sodium filling the upper-half of gap under 1st leg of SP
SP+sodium(down,2nd)	SP and sodium filling the lower-half of gap under 1st leg of SP and sodium filling the gap under 2nd leg of SP
SP+sodium(2nd)	SP and sodium filling the gap under 2nd leg of SP
SP+sodium(up,down,2nd)	SP and sodium filling the gap under both 1st leg and 2nd leg of SP
SP+sodium(up,down,2nd)+defect(A)	SP and sodium filling the gap under both 1st leg and 2nd leg of SP and defect in position "A" under SP
SP+sodium(up,down,2nd)+defect(B)	SP and sodium filling the gap under both 1st leg and 2nd leg of SP and defect in position "B" under SP
SP+sodium(up,down,2nd)+defect(A) half filled	SP and sodium filling the gap under both 1st leg and 2nd leg of SP and defect in position "A" under SP (the defect is 50% filled with sodium)
SP+sodium(up,down,2nd)+defect(A) completely filled	SP and sodium filling the gap under both 1st leg and 2nd leg of SP and defect in position "A" under SP (the defect is 100% filled with sodium)

The 3D-RFECT code [8,11-12] is based on the finite element method and a reduced magnetic vector potential with nodal elements discretization. The Coulomb gauge is not explicitly imposed but added as a medium null value using a penalty factor, as shown in [13], which provide a unique solution when the magnetic vector potential decreases to zero on the FEM volume boundary. The code uses for accurate ECT signal calculation 2nd order tetrahedron. By using the reduced vector potential, the source of the field is not added in the FEM model, but as an additional term in the external source field in all nodal points of the FEM volume, which are calculated based on Biot-Savart law.

FEM numerical simulations of the distribution of the magnetic vector potential, using the 3D-RFECT code, is illustrated for the case of the large SP with multiple SG tubes in Fig. 5 and 6. In Fig. 5, the RF-ECT sensor is located in a peripheral SG tube while in Fig. 6 the sensor is located in the central SG tube which is completely surrounded by other 8 tubes. The excitation sensor locations in the RF-ECT system correspond to the red zone on the tube while the sensor location is between them. It can be seen that in the area corresponding to the reception sensor location, the magnetic vector potential decreases as the coil moves from the non-central SG tube (Fig. 5) to the central SG tube (Fig. 6). Simulations of the amplitude of SP signal and field visualization [10] show that there is a shielding electromagnetic effect due to surrounding SG tubes, that is decreasing the signal from SP by up to 20% [11-12].

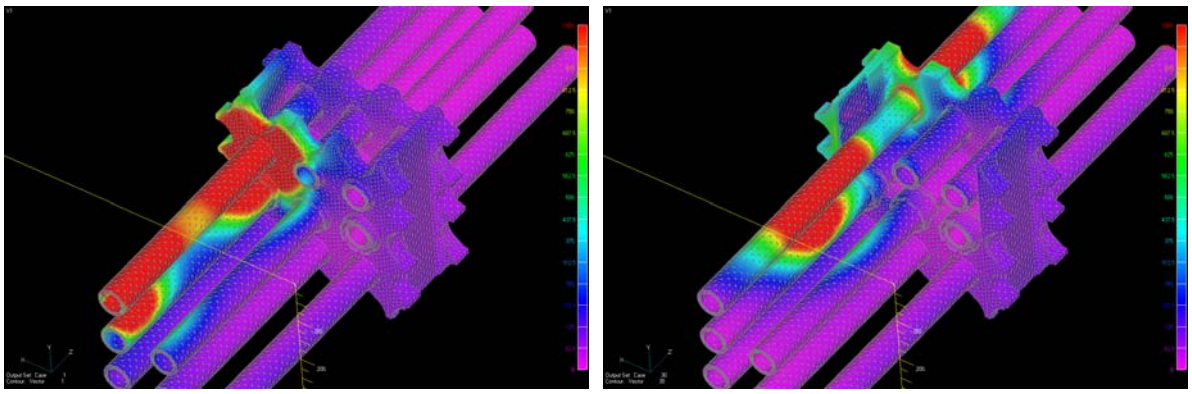

Fig. 5. Simulation of distribution of the magnetic vector potential when RF-ECT sensor inspect from a peripheral SG tube

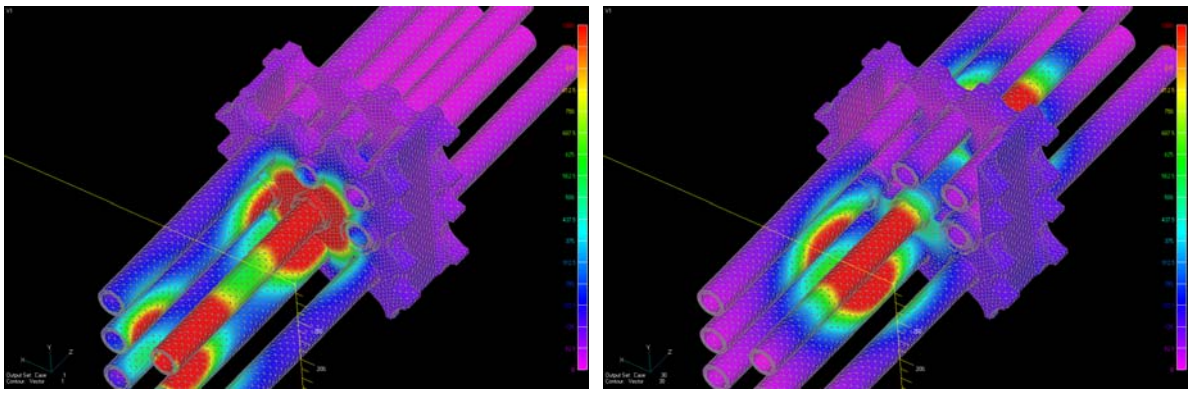

Fig. 6. Simulation of distribution of the magnetic vector potential when RF-ECT sensor inspect the SG tube located in the middle of SP and surrounded by other eight SG tubes

FEM simulations were performed using the 3D-RFECT code by employing 2nd order

tetrahedrons in a nodal implementation for a reduced magnetic vector potential [13]. The FEM mesh consisted in 3,000,000 second order tetrahedrons with 4,000,000 nodes. The generated assembled FEM matrix has a size of 24,000,000 with 725,000,000 non-zero real values in the sparse matrix. Numerical simulation were performed by moving the probes in 150 steps separated by 2mm, each of them representing a different computation. The total computation time for each run using 1024 CPUs on BX900 PRIMERGY Fujitsu supercomputer [14,15] was between 2-3 hours, depending on the convergence rate (10^{-6} precision after 1000-2000 iterations using a bi-conjugate gradient solver) in the iterative solver for each specific case. The parallel computation is using 8 cores (2 quad Intel Xeon X5570) per node with OpenMP parallelization between cores on each node and a total of 128 nodes with MPI parallelization between nodes. The maximum memory required for the program to run is 16 GB per node. The minimum requirement of the solver to run the above configuration is 2 nodes or 16 CPUs and 32 GB of memory.

3. Simulations of multi-frequency RF-ECT algorithms for ISI of SG tubes

In the multi-frequency ECT algorithm [16] two detection signals of the RF-ECT sensor at different frequencies are combined in order to minimize the noise in the signal. If we consider that signal at frequency v_1 is C_1 and signal at frequency v_2 is C_2 , then the multi-frequency algorithm first map the signal C_2 at frequency v_2 to a new signal C_3 but at frequency v_1. The multi-frequency signal S is then computed after reducing the initial signal C_1 by the mapped signal C_3. Each signal (C_1, C_2 and C_3) have two components related to the resistive and inductive components respectively.

Equation (1) shows the steps of the multi-frequency algorithm for two frequencies and using a linear mapping that depends on two parameters: amplitude amplification k and signal phase rotation α. The choice of the mapping algorithm depends on the variation of signals C_1 and C_2 with frequency. In the present paper, the mapping is related to parameters that modify the shape of the signals in the Lissajous representation and do not perform on each individual point of the Lissajous curve. Fig. 7 shows a graphical representation of the multi-frequency algorithm described by Equation (1).

$$
\begin{aligned}
&C_1 = (x_1^i, y_1^i),\ C_2 = (x_2^i, y_2^i),\ C_3 = (x_3^i, y_3^i),\ i = 1,n \\
&\begin{pmatrix} x_3^i \\ y_3^i \end{pmatrix} = k \begin{pmatrix} \cos\alpha & -\sin\alpha \\ \sin\alpha & \cos\alpha \end{pmatrix} \begin{pmatrix} x_2^i \\ y_2^i \end{pmatrix} \\
&S = \begin{pmatrix} x_1^i \\ y_1^i \end{pmatrix} - \begin{pmatrix} x_3^i \\ y_3^i \end{pmatrix} \quad \textit{- multi - frequency signal}
\end{aligned}
\tag{1}
$$

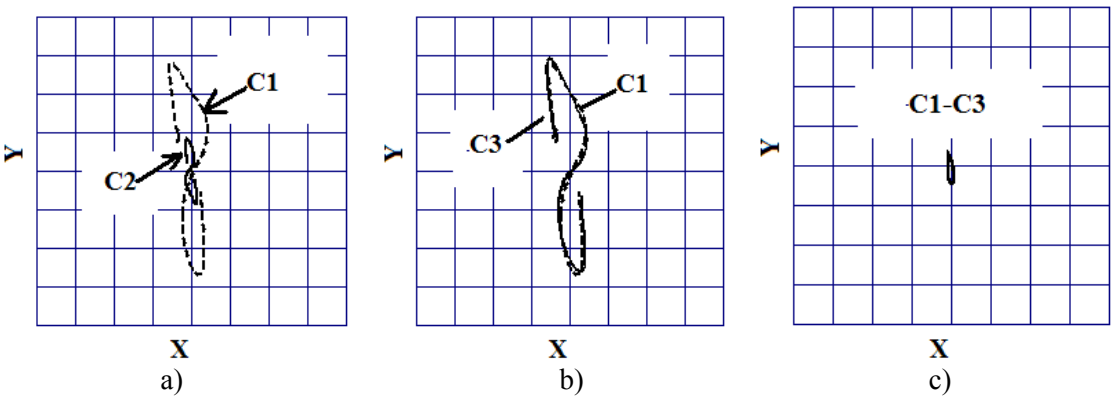

Fig. 7. Schematic of the multi-frequency ECT technique: a) initial signals at two different frequencies; b) mapping of signal from one frequency to the other; c) multi-frequency signal

For example, in the ISI using ECT of a SG support plate, C_1 and C_2 are the recorded ECT signal of support plate at frequency v_1 and v_2, respectively. At first step, the signal C_3 is constructed only by amplifying and rotating the signal C_2 in that way that is became as close as possible to the signal C_1. In the multi-frequency algorithm, the SP signal is represented by the difference between signal C_1 and C_3 which depends only on two parameters (amplification k and rotation α) that can be calculated in the absence of any defect close to SP. Determination of the multi-frequency parameters (amplification k and rotation α) are done therefore in the absence of any defect and they result from the minimization of the maximum distance between all points of curve C_1 and C_3. In multi-frequency algorithm, the minimum difference (*C1-C3*) represents the noise after SP was reduced.

In the ISI of FBR SG tubes, the signal of noise is considered to be the combined signal from tube SP and sodium. Because of the non-linear effect of the sodium to the RF-ECT signal, the mapping of the multi-frequency algorithm is based on a linear algorithm, which is more robust against unknown non-linear behavior of input signals. However, because there are variations in the SP signal due to sodium filling the air-gap between SP and SG tube, for each sodium form, a multi-frequency algorithm can be determined to reduce to a minimum the SP signal. Among all multi-frequency algorithms, it is chosen the one that minimize the difference (C_1-C_3) for all sodium forms.

The multi-frequency algorithm assumes that there is a smaller modification of the SP signal when frequency changes from v_1 to v_2 compared with that of the defect under SP, and that SP signal has a more linear behavior with frequency. By combining the signal from cases with defects and cases without defects, the optimum multi-frequency algorithm is the one that is able to provide the higher Signal/Noise ratio after it was applied to the most conservative models with and without sodium and defects under SP.

Because in ISI of FBR SG tubes the multi-frequency algorithm parameters are determined from the constraints to minimize all noise arising from sodium next to SP, the algorithm does not depend on sodium signal or variations in SP signal. If the multi-frequency algorithm is applied to a signal from a SP which was an unknown sodium distribution and the multi-frequency signal (C_1-C_3) exceed by a factor of 2 the maximum noise of multi-frequency algorithm, then this is an indication of a hidden defect near SP filled partially with sodium.

3.1. SP and sodium signal

Numerical FEM simulations were conducted to analyze the effect of sodium to SP signal, when sodium builds up in the gap between SP and tube. Fig. 8 shows an increase of the SP signal due to sodium, in all sodium configurations. The largest change of SP signal is when sodium is filling 100% the gap between SP and tube at both inspection frequencies: 150 and 450 Hz. Also, it can be noticed that addition of sodium under the 2nd leg of SP has a large influence of the SP signal. Because the sodium filling factor cannot be controlled during sodium draining, numerical simulations looked for the worst scenario, and Fig. 8 shows the maximum variation of the SP signal due to sodium for the single SG tube case. The location of the 1st leg and 2nd leg of SP corresponds to the peak in the signal at distance 100 mm, and 200 mm respectively. The starting scanning point indicated by "0" in Fig. 8 is 100 mm far from the edge of 1st leg of SP. Fig. 9 shows the SP signal in similar conditions as in Fig. 8, but for the case of large SP with multiple (nine) SG tubes. This result corresponds to the situation when the sensor enters in the central SG tube (Fig. 6). Again, at both 150 Hz and 450 Hz frequencies, the maximum sodium noise is when sodium fills completely the gap between SP and SG tube.

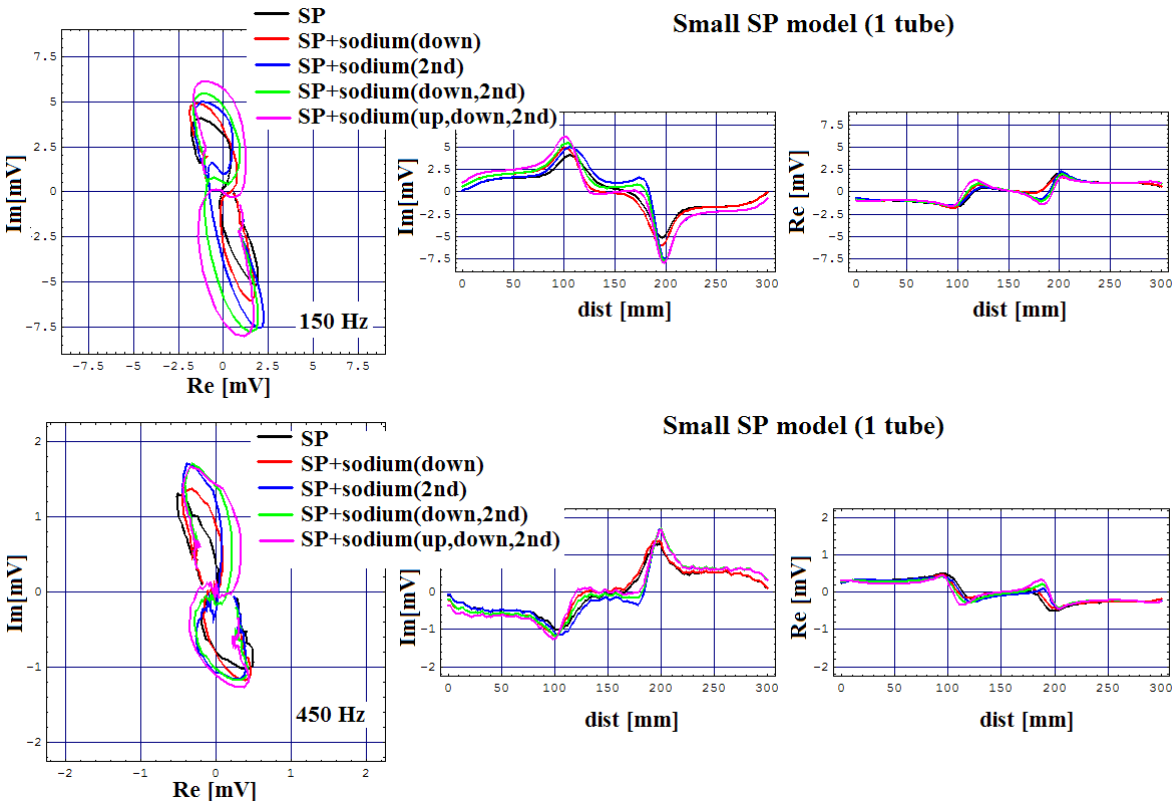

Fig. 8. Signals for SP with/without sodium for the small SP with single SG tube

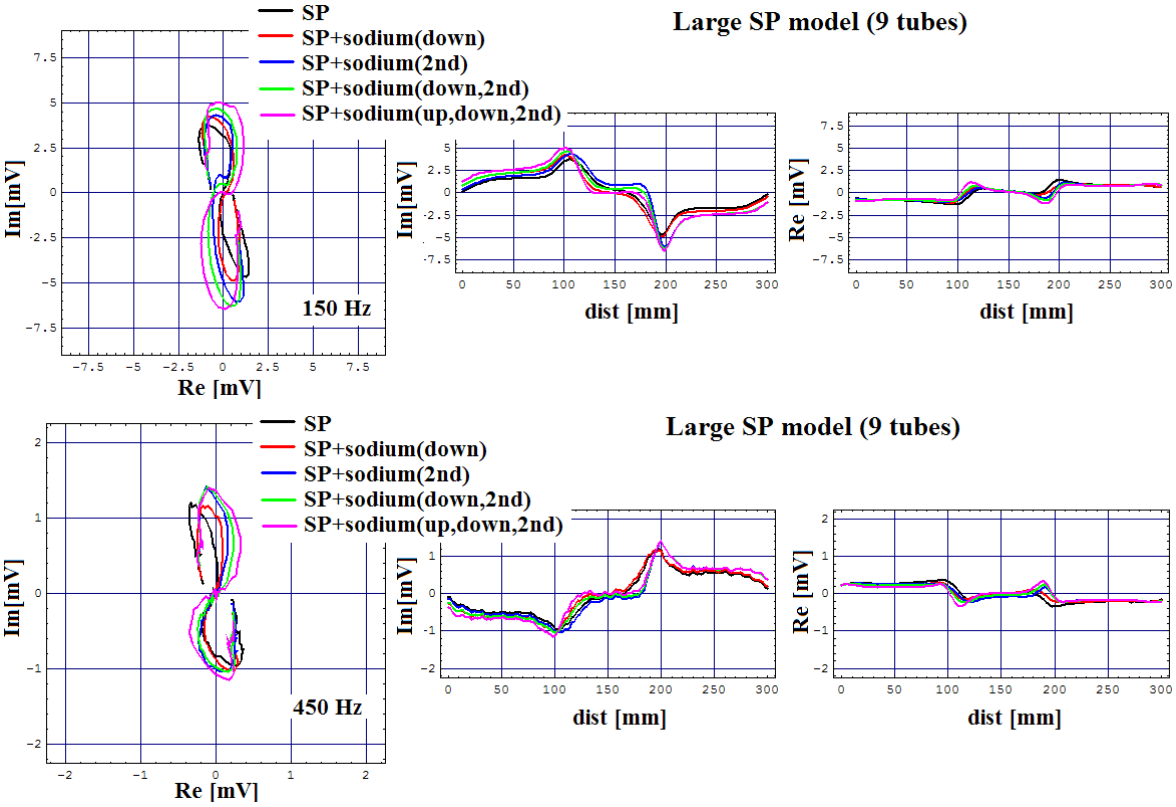

Fig. 9. Signals for SP with/without sodium for the large SP with nine SG tubes

By comparing the SP signal from the large SP case to that of the small SP one, it can be seen that there is a 10-20% signal reduction in all cases with or without sodium, which is due to the electromagnetic shielding of surrounding SG tul he reduction effect is similar for all cases and should not be interpreted as the influence of a l 63 ı defect under SP. Later results will show that while the overall SP signal decreases, the signal/noise ratio of the defect indication remains constant or even increases. However, this aspect should be taken into consideration when results are compared and interpreted starting from experimental evidence in a SG mock-up and actual measurements during inspection of FBR SG tubes.

SP signal amplitude and phase variations between the single tube and multiple tubes cases are listed in Table 3 and Table 4 for both 150Hz and 450Hz.

Table 3 Variations in the amplitude-phase of SP signal at 150 Hz

Description	*Small SP (1 tube) (ampl[mV]-phase[deg])*	*Large SP (9 tubes) (ampl[mV]-phase[deg])*	*Variation ([%]-deg)*
SP	(9.79 - 109.51)	(8.74 - 105.55)	(10.73 - 3.96)
SP+sodium(down)	(11.39 - 106.48)	(9.22 - 99.31)	(19.05 - 7.17)
SP+sodium(2nd)	(12.91 - 105.28)	(10.44 - 96.25)	(19.13 - 9.03)
SP+sodium(down,2nd)	(13.5 - 101.31)	(10.99 - 94.79)	(18.59 - 6.52)
SP+sodium(up,down,2nd)	(14.32 - 99.14)	(11.51 - 92.37)	(19.62 - 6.77)

Table 4 Variations in the amplitude-phase of SP signal at 450 Hz

Description	*Small SP (1 tube) (ampl[mV]-phase[deg])*	*Large SP (9 tubes) (ampl[mV]-phase[deg])*	*Variation ([%]-deg)*
SP	(2.52 -67.8)	(2.25 -73.65)	(10.71 - 5.85)
SP+sodium(down)	(2.67 -72.35)	(2.21 -80.06)	(17.23 - 7.71)
SP+sodium(2nd)	(2.95 -76.85)	(2.46 -83.14)	(16.61 - 6.29)
SP+sodium(down,2nd)	(2.95 -77.07)	(2.46 -83.47)	(16.61 - 6.4)
SP+sodium(up,down,2nd)	(3.01 -76.12)	(2.57 -84.05)	(14.62 - 7.93)

3.2. Multi-frequency to suppress SP and sodium signal

As it was mentioned in the previous section, the multi-frequency algorithm aims to suppress both SP and sodium signal by combing the RF-ECT signals at two different frequencies. Because of the uncertainty in sodium percentage filling the gap between SP and tube, it was considered a linear algorithm which is expected to be more robust to the sodium noise distribution. In the present analysis the noise is due to sodium and its non-linear electromagnetic interaction with both tube and SP.

While this algorithm is validated with the worst case scenario for sodium noise through numerical simulations, it is required for it to work also with experimental data, where additional noise sources not included in the present analysis are present.

The parameters defining the multi-frequency algorithm are defined by the amplification factor k and phase rotation α, as shown previously in Equation (1). Those parameters are determined separately for each model: small SP or large SP with/without sodium, in order to assess the validity of extrapolating the algorithm from the small SP case to the large SP case. The values are determined in such way that the resulting signal from multi-frequency algorithm (S) has the minimum amplitude.

While small variations are found in multi-frequency parameters when the analysis is shifted from the small SP model to the large SP model, addition of sodium has a large effect on the amplification factor. That suggests that optimum multi-frequency algorithms should be determined by

including sodium in the analysis from the beginning.

In the following, only the optimum algorithm determined for each case and its applicability to the most complex case of large SP with multiple tubes (closer to actual FBR inspection) are considered.

Table 5 Parameters of the linear multi-frequency algorithm to suppress SP and sodium signal

Case	*Amplitude amplification k*	*Phase α [deg]*
1 tube - SP	3.81	177.31
1 tube - SP+sodium(up,down,2nd)	4.75	175.26
9 tubes -SP	3.89	179.2
9 tubes -SP+sodium(up,down,2nd)	4.17	179.37

3.3. Analyses for small SP model with 1 Tube, no sodium

In the first analysis we start from the model of the small SP with single SG tube. Numerical simulations of the ISI of an FBR SG tube with a defect located in position "A" (Fig. 2) are shown in Fig. 10 at both 150Hz and 450 Hz. The defect is an outer groove full circumferential 10 mm wide and depth 50%tw from tube wall thickness. The additional electromagnetic signal due to the presence of such defect against the signal of SP shows the strongest variation around defect position, under 1st leg of SP, and also indicates a small variation under 2nd leg of SP. At higher frequency, 450 Hz, the phase of signal due to presence of the defect is changing significantly by more than 60 degrees.

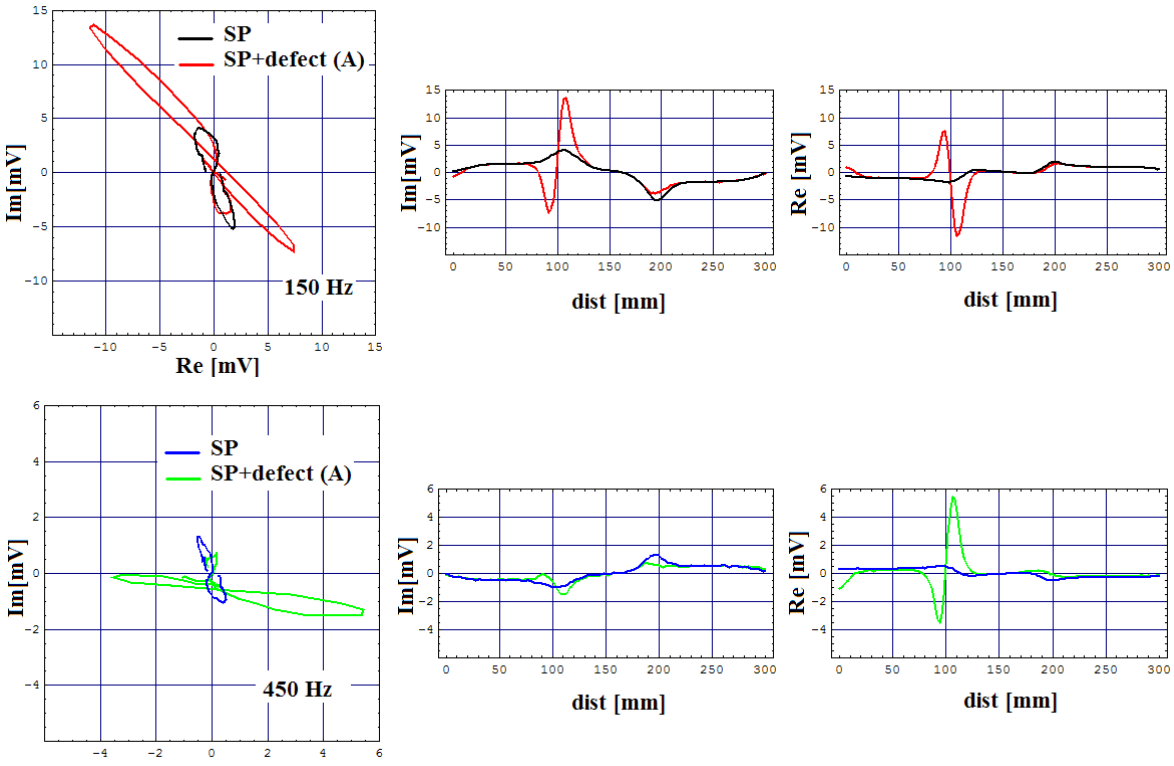

Fig. 10. ECT signal at 150 Hz , 450 Hz from OD 50%tw in position "A" under small SP

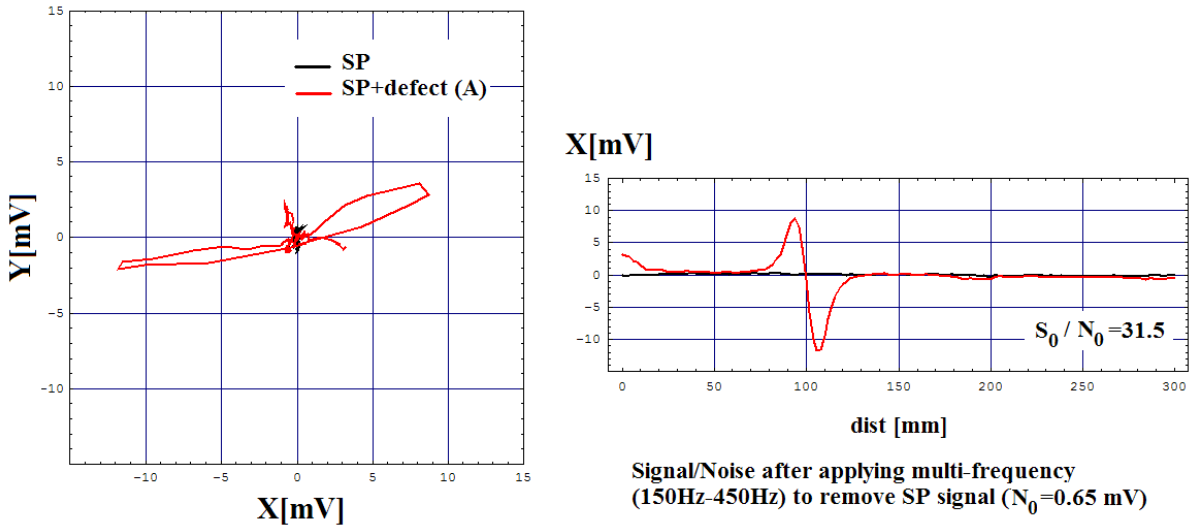

Fig. 11. Enhancement of the OD50%tw, position "A", signal after applying multi-frequency algorithm and suppressing SP signal

The most optimum multi-frequency algorithm, determined on the constrain of minimum value of amplitude, shows a very high value 31.5 of Signal/Noise (S_0/N_0) ratio, where noise N_0 (0.65 mV) is represented only by SP signal and signal S_0 is the signal recorded when there is a defect under SP (see Fig. 11).

3.4. Analyses for small SP model with 1 Tube, with sodium

The second analysis concerns the model of the small SP and a single SG tube in the presence of sodium. The maximum variation of SP signal due to different sodium distributions is simulated and presented in Fig. 12 at 150Hz and 450 Hz. The larger signal variation is for 100% sodium filling of the gap between SP and tube, both under 1st and 2nd SP legs.

The best multi-frequency algorithm in minimizing the combined noise of both SP and sodium gives a maximum noise N_0=1.6mV, which is higher than in the previous case without sodium (see Fig. 13). The algorithm was determined separately, specific for the case when sodium is present.

Simulations of the SP signal and an outer groove defect (OD50%tw, 10 mm wide) under SP in position "A" are shown in Fig. 14, when the defect is either empty of filled 50% with sodium. For large defects the signal from defect decreases as the defect fills up with sodium.

Application of the multi-frequency algorithm (Table 5, line 2) in order to suppress SP and sodium noises results in a signal/noise ratio of 6.3 when defect is empty and a signal/noise ratio of 3.6 when the defect is filled 50% with sodium (Fig. 15). The decrease of the S_0/N_0 ratio is due to noise increase because of the sodium interaction with SP and tube.

In the quest for determining the best multi-frequency algorithm, the final criteria is to have the highest signal/noise ratio which might or not correspond to the criteria of smaller noise, due to the non-linear interaction effect of sodium. Variations in the multi-frequency algorithm parameters are obtained by tuning the algorithm to minimize the noise from specific sodium structures (such as sodium(up), sodium (down), sodium (up, down) and others), then applied to all the other cases to find the overall maximum possible noise N_0 (see Table 6). It can be seen that the smallest noise N_0 is not obtained when starting the tuning from the configuration of sodium which provides the highest variation of the SP signal which is "sodium (up, down, 2nd)". This is because a high signal of SP does not necessarily imply a small noise N_0 in the multi-frequency algorithm. In other words, a smaller radius of distribution of values of noise N_0 is obtained by starting multi-frequency algorithm from a

point where sodium filling is not extreme but is closer to all cases generated when starting from 0% to 100% sodium filling. Because of the non-linearity of the problem and no-trivial solution, determination of the optimum parameters has be done trough trial and error analysis of all possible sodium combinations, through numerical simulations.

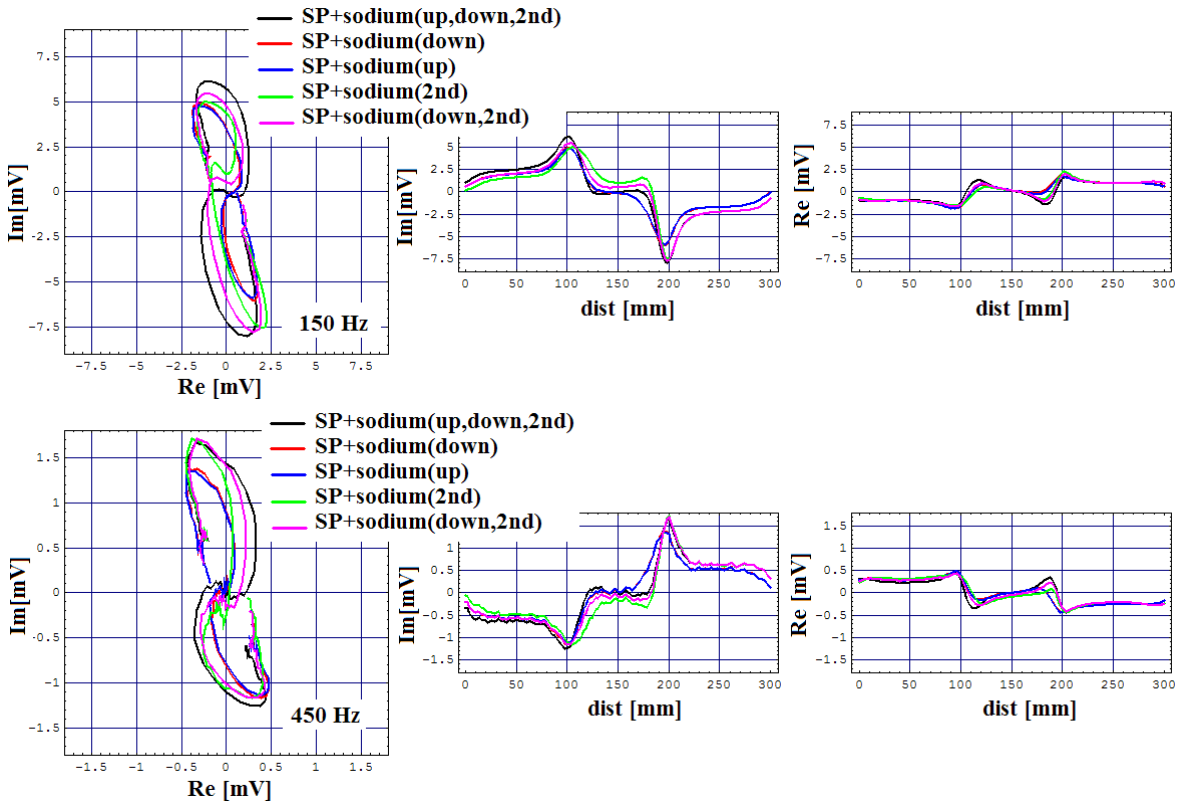

Fig. 12. ECT signal at 150 Hz and 450 Hz from sodium in the small SP model

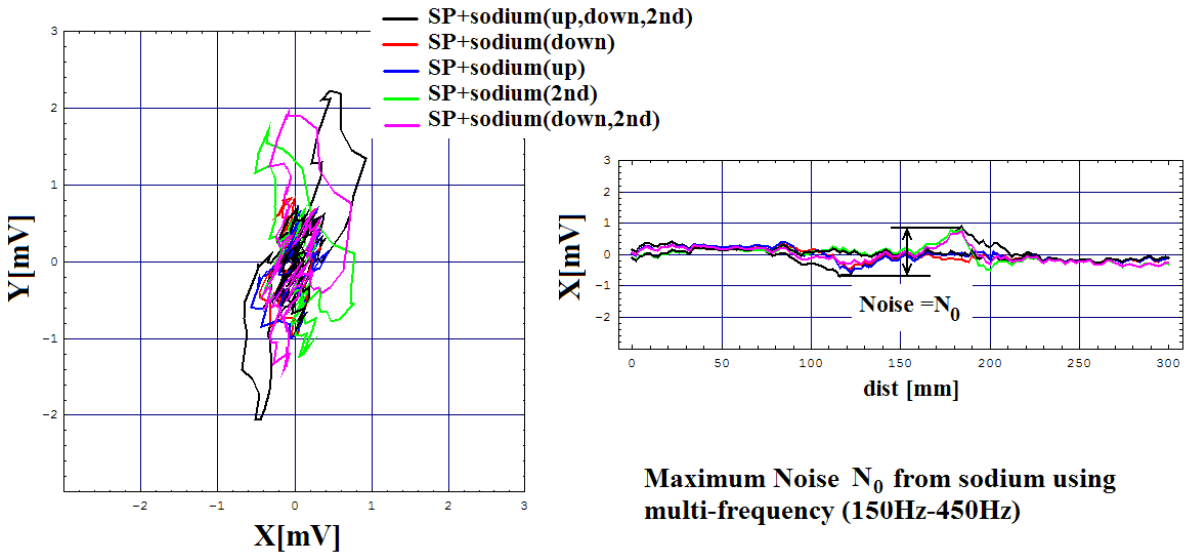

Fig. 13. Maximum noise N_0 (1.6 mV) from sodium using the multi-frequency algorithms derived from case "1 tube-SP" without sodium (as shown in Table 5)

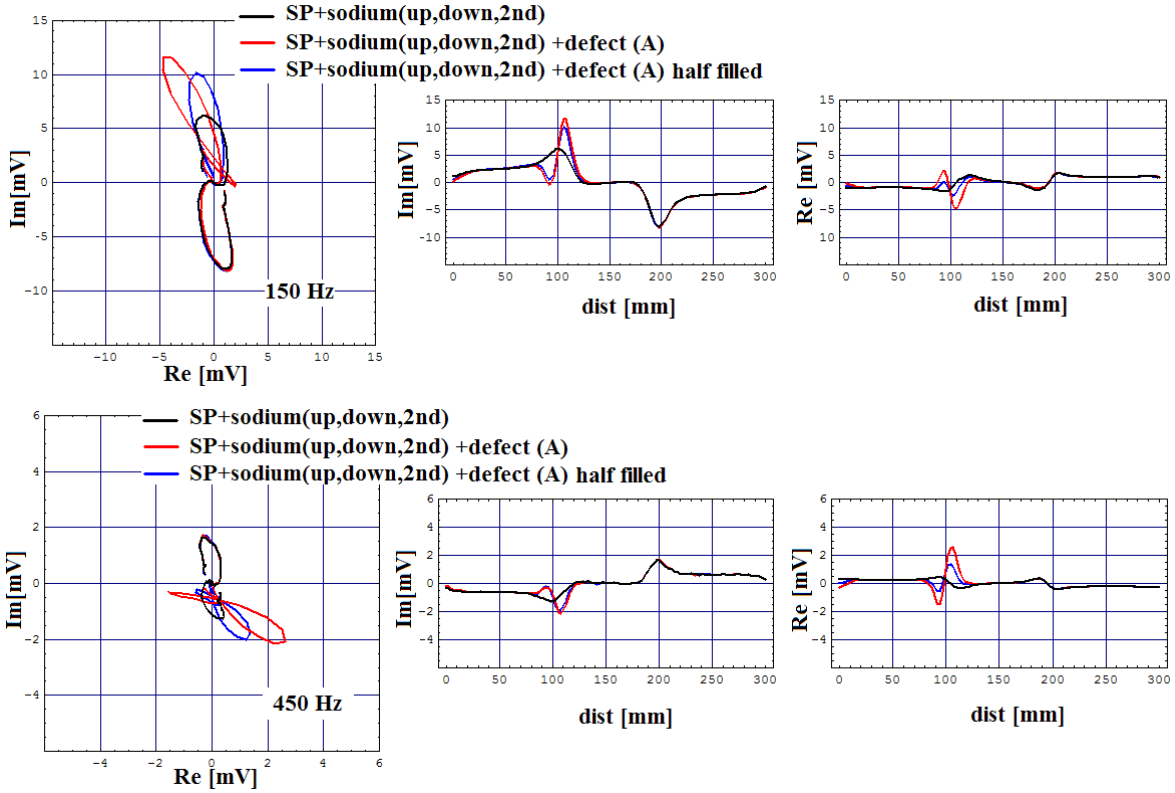

Fig. 14. ECT signal at 150 Hz and 450 Hz from OD 50%tw in position "A" under the small SP model

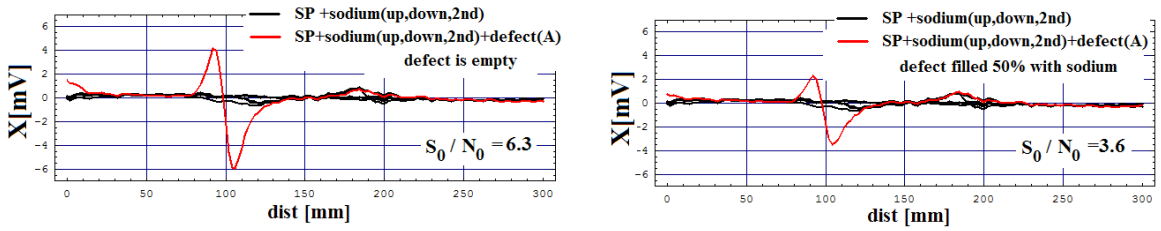

Fig. 15. Multi-frequency algorithm using parameters from case "1 tube-SP" for OD50%tw, position "A", after removing SP and sodium signal

Table 6 Variations in the parameters of the multi-frequency algorithm to suppress SP signal and sodium (1 tube, small SP model)

Case	*Amplitude amplification k*	*Phase α [deg]*	*Sodium noise N [mV]*
SP+sodium(up,down,2nd)	4.75	175.26	2.23
SP+sodium(down)	4.27	178.84	1.6
SP+sodium(up)	4.26	177.18	1.91
SP+sodium(2nd)	4.37	182.13	1.64
SP+sodium(down,2nd)	4.57	178.38	1.58

As an example of the previous discussion, the multi-frequency algorithm was analyzed by starting from the point corresponding to the one with "sodium(up, down, 2nd)" which has the strongest influence (SP has the largest amplitude variation) of the SP signal, as shown in Fig. 12. The maximum noise obtained from the multi-frequency algorithm (whose parameters are listed in Table 6, line 1) is N=2.23 mV (Fig. 16).

Detection of an empty defect or a defect filled 50% with sodium (Fig. 17) shows smaller values of signal/noise ratio than those obtained in Fig. 15, in which the starting point of minimization was using an SP with sodium, but in the absence of any defect.

The best results however are obtained when the starting point in the multi-frequency algorithm is given by the combination of sodium under 1st and 2nd leg, and are represented by the case "sodium (down, 2nd)". The minimum noise N obtained is 1.58 mV (Fig. 18). The multi-frequency algorithm for the detection of defect in position "A", not filled or filled 50% with sodium increases to S/N=7.45 and S/N=3.95, respectively (Fig. 19).

As a conclusion, the best multi-frequency algorithm is the one which starts from a k-α point that is closer to the centroid of all the optimum k-α pairs obtained from the different sodium distributions. Therefore, computation of additional sodium accumulation shapes could provide even better S/N ratios.

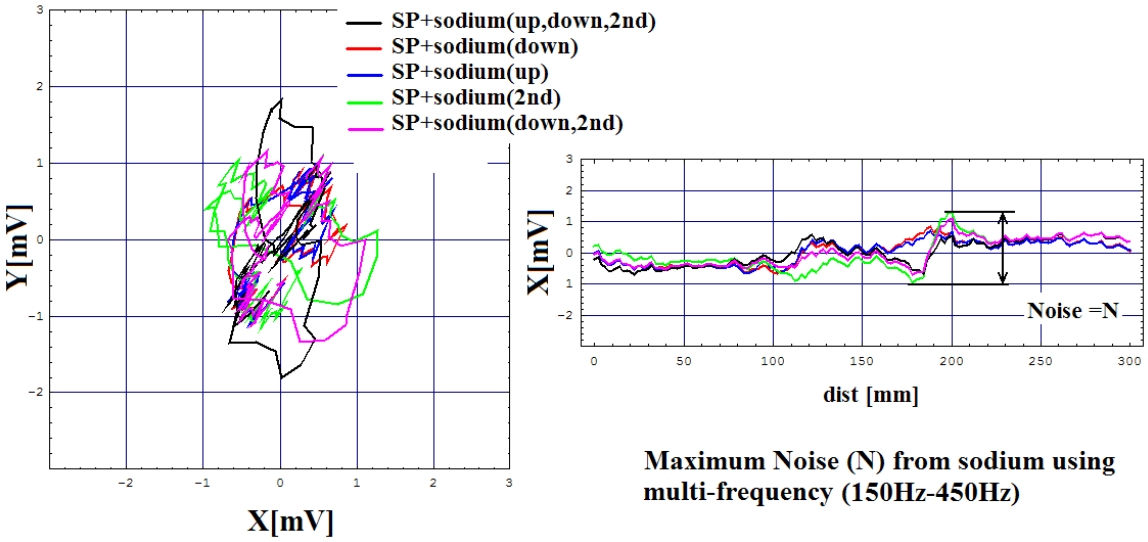

Fig. 16. Maximum noise N (2.23 mV) from sodium using multi-frequency algorithm derived from case "SP+sodium(up, down, 2nd)" with sodium (as shown in Table 6)

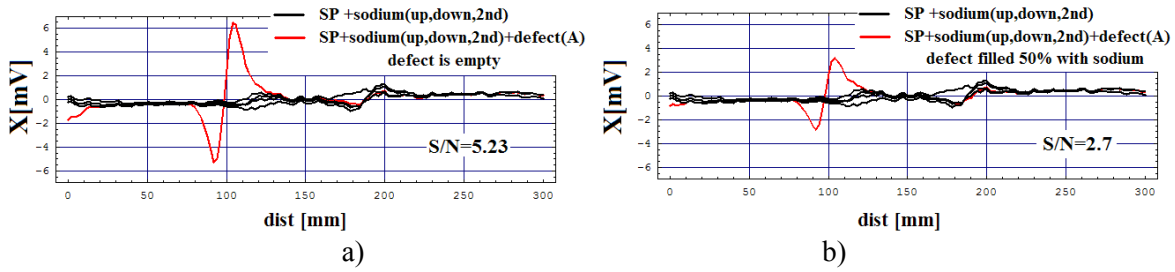

Fig. 17. Multi-frequency algorithm using parameters from case "SP+sodium(up, down, 2nd)" for OD50%tw, position "A", after removing SP and sodium signal

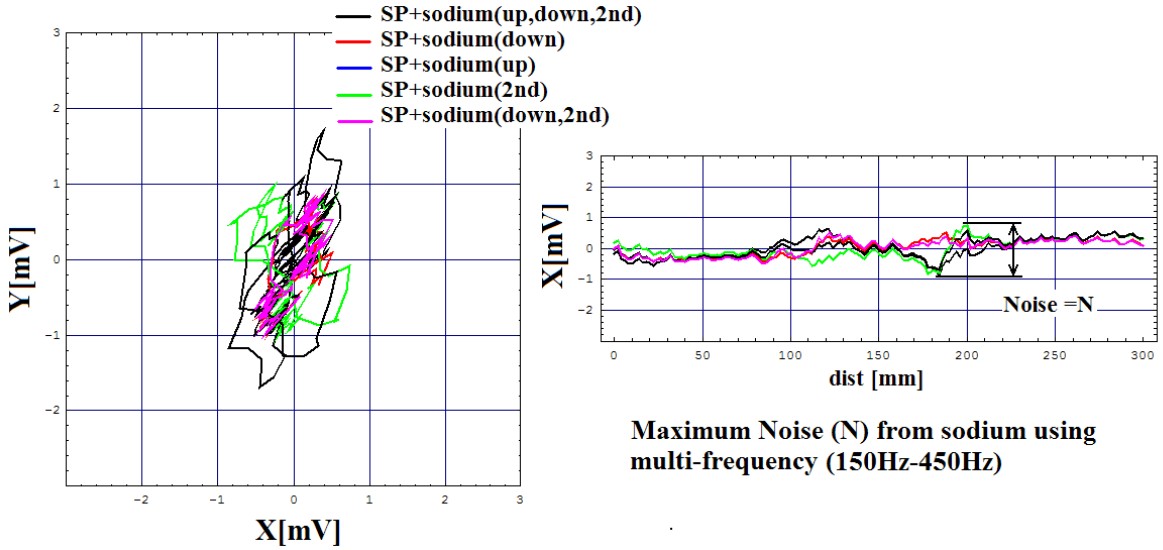

Fig. 18. Maximum noise N (1.58 mV) from sodium using multi-frequency algorithm derived from case "1 tube-SP+sodium(down, 2nd)" with sodium (as shown in Table 6)

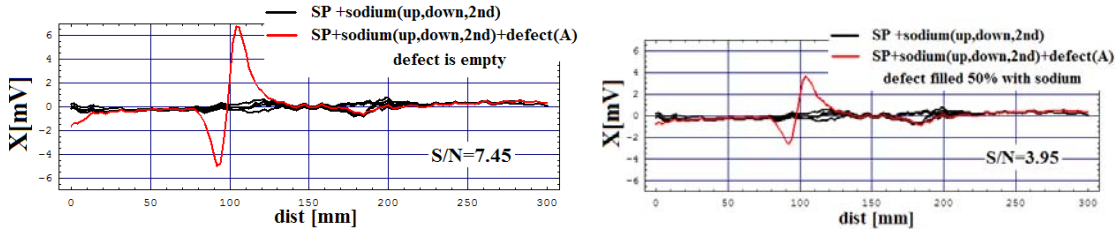

Fig. 19. Multi-frequency algorithm using parameters from case "1 tube-SP+sodium(down, 2nd)" for OD50%tw, position "A", after removing SP and sodium signal

3.5. Analyses for large SP model with 9 Tubes, no sodium

In the next stage the analysis is focused on the case with large SP and multiple SG tubes. Previous numerical analysis showed that signal of SP is decreased by 20% in comparison with the single tube case [14]. However, because the multi-frequency analysis is a result of mixing the signal at different frequencies, it does not automatically imply that S/N ratio should also decrease.

Another aspect of the simulation concerns the applicability of optimum multi-frequency algorithms that were obtained in the case of small SP to the case of large SP. Previously, it was already seen that application of algorithm from "no-sodium" to "sodium" could worsen the S/N ratio .

Fig. 20 shows the variation of SP signal with a defect in position "A" (shown in Fig. 2) for the large SP model with nine SG tubes. The simulation results correspond to the inspection of SG tubes in the central position of the assembly.

In Fig. 21 the multi-frequency algorithm obtained in the case of "small SP, 1 tube" (Table 5, line 1) is applied to the case of "large SP, 9 tubes". The noise N_0 remains low at 0.77 mV and the signal/noise ratio decreases from 31.5mV to 28.6mV but remains very large. At this point, for ISI of FBR SG tubes, simulations show applicability of the multi-frequency algorithm obtained from data of

"small SP, 1 tube" to the signal of "large SP, 9 tubes" is well proven, and do not pose any serious concerns.

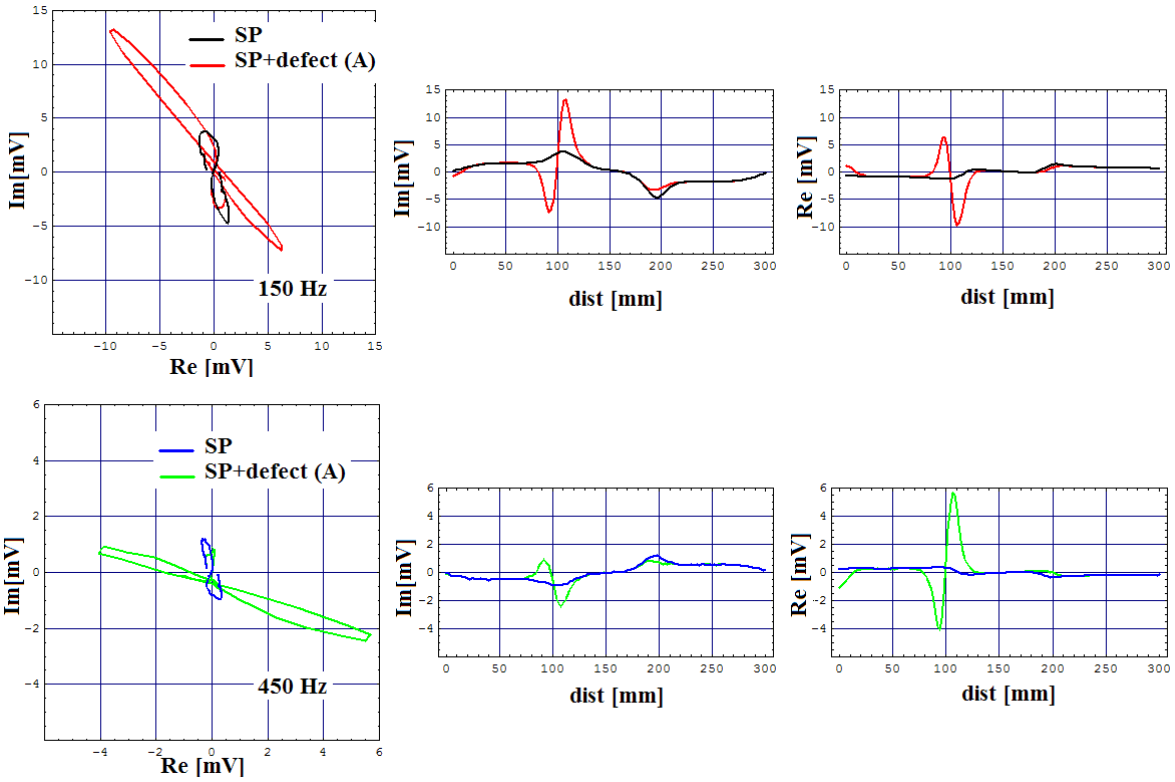

Fig. 20. ECT signal at 150 Hz and 450 Hz from OD 50%tw in position "A" under large SP model with 9 tubes

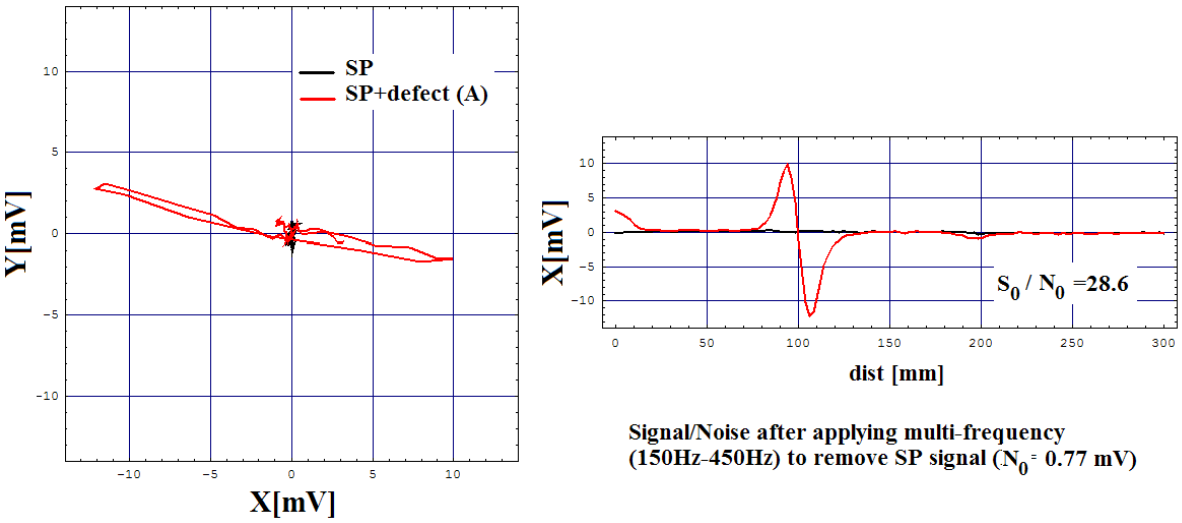

Fig. 21. Multi-frequency algorithm using parameters from case "1 tube-SP" for OD50%tw in position "A" after removing SP

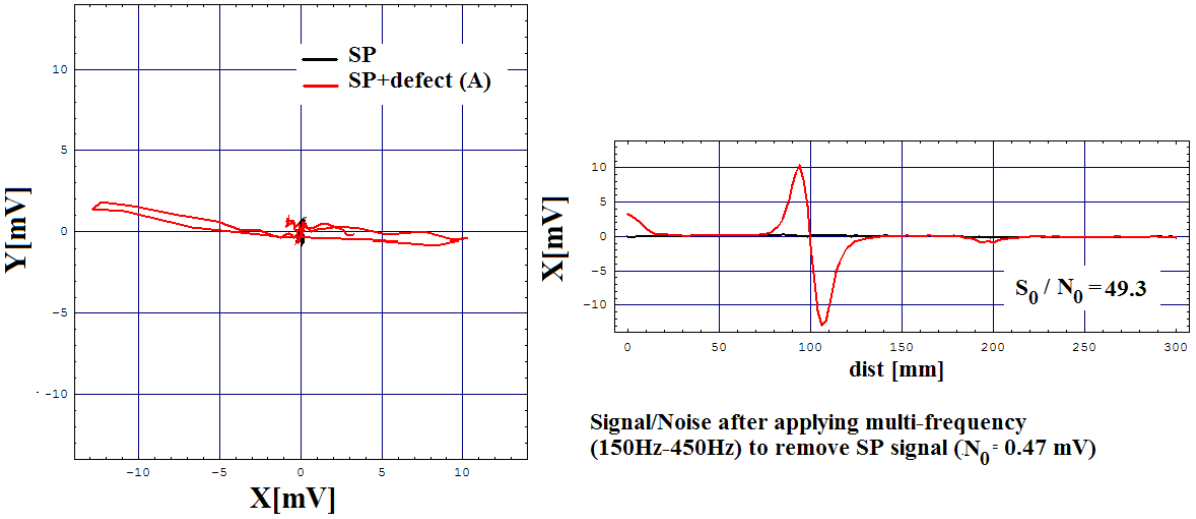

Fig. 22. Multi-frequency algorithm using parameters from case "9 tubes-SP" for OD50%tw after removing SP (noise N_0=0.47 mV)

However, a much better multi-frequency algorithm could be determined if the analysis was performed using numerical simulations of "large SP, 9 tubes" with the parameters of the algorithm listed in Table 5, line 3. Fig. 22 shows the better performance of such algorithm, with a higher signal/noise ratio S_0/N_0 of 49.3. Higher signal/noise ratio values were obtained because of a reduction in noise level. Also, as pointed earlier, the multi-frequency algorithm performance is not related to the amplitude of the signals at different frequencies but to the ratio of those signals, as well as to the distribution of noise around the SP and defect signals, and therefore multi-frequency algorithm performance is different than when using ECT signals at various frequencies.

Numerical simulations showed that while there is a decrease of 20% of amplitude of SP signal due to the electromagnetic shielding of surrounding tubes, the multi-frequency algorithm is actually providing better signal/noise ratio due to a better distribution of SP noise with frequency.

3.6. Analyses for large SP model with 9 Tubes, with sodium

In the last analysis, the most complex model of "large SP with 9 tubes" with sodium is taken into consideration, because this is the closest approximation to actual ISI of FBR SG tubes.

As in previous sections, the feasibility of applying the multi-frequency algorithms determined in the case of "small SP , 1 tube with sodium" has to be validated. Fig. 23 shows the simulated signal when defect position is "A" or "B" (shown in Fig. 2)and the defect is either 50% or 100% filled with sodium at 150Hz and 450Hz.

Several multi-frequency algorithms were determined starting from several sodium distributions, and the respective parameters are listed in Table 7. As in the "small SP, 1 tube" case, the smallest noise N_0 is not obtained by starting from "sodium (up, down, 2nd)" which has the highest influence of the SP signal but from the case "sodium (down, 2nd)".

In Fig. 24, the multi-frequency algorithm that was determined for the model "small SP, 1 tube no sodium" is applied to the large model, and its parameters are listed in Table 5, line 1. The maximum noise level is N_0=1.3mV.

The detectability of defects and corresponding signal/noise ratio by applying this algorithm is shown in Fig. 25. It can be noticed that higher signal/noise ratios are obtained for defects in position "B" than for defects in position "A". Also, it can be observed that filling of the defects with more than

50% of sodium does not change the signal/noise ratio S_0/N_0 of 3.12. This proves the stability of the algorithm against unknown sodium filling. At last, comparison with the signal/noise ratio from cases of "small Sp, 1 tube with sodium" (Fig. 19) shows a small reduction from 3.95 to 3.13. However, we have to remind that the applied algorithm is not optimized for this configuration, but determined from the case of "small SP, 1 tube without sodium".

Despite the slight decrease in the signal/noise ratio, numerical analysis showed that it is possible to apply the algorithm determined in case of "small SP, 1 tube no sodium " to the data of "large SP, 9 tubes with sodium", but it is not the optimum solution, as it will be shown later.

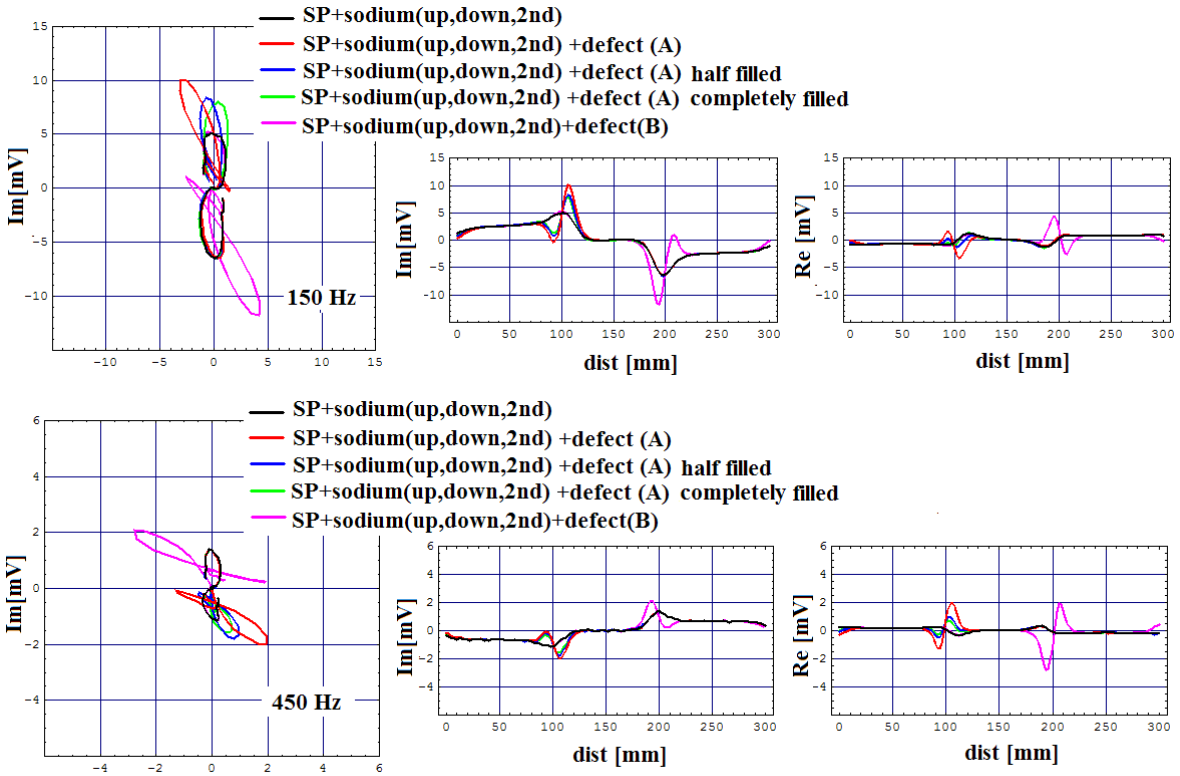

Fig. 23. ECT signal at 150 Hz and 450 Hz from OD 50%tw in position "A", "B" under the large SP model with 9 tubes

Table 7 Variations in the parameters of the multi-frequency algorithm to suppress SP and sodium signal (9 tubes, large SP model)

Case	*Amplitude amplification k*	*Phase α [deg]*	*Sodium noise N [mV]*
SP+sodium(up,down,2nd)	4.49	176.42	1.46
SP+sodium(down,2nd)	4.46	178.27	1.15
SP+sodium(down)	4.17	179.37	0.96
SP+sodium(2nd)	4.24	179.39	1.64

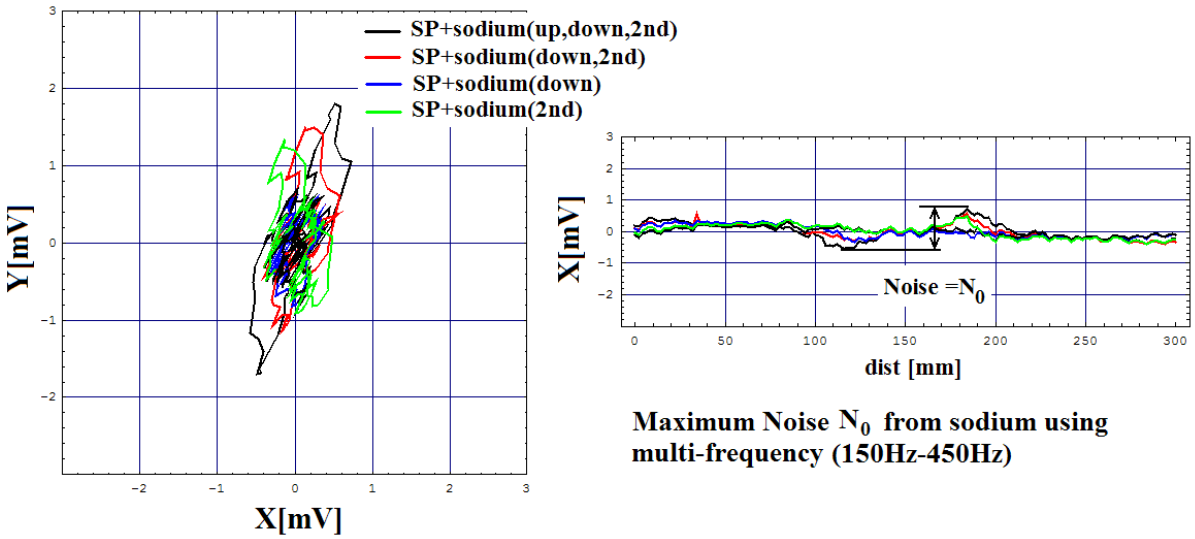

Fig. 24. Maximum noise N_0 (1.3 mV) from sodium using the multi-frequency algorithms derived from case "1 tube-SP" without sodium (as shown in Table 5)

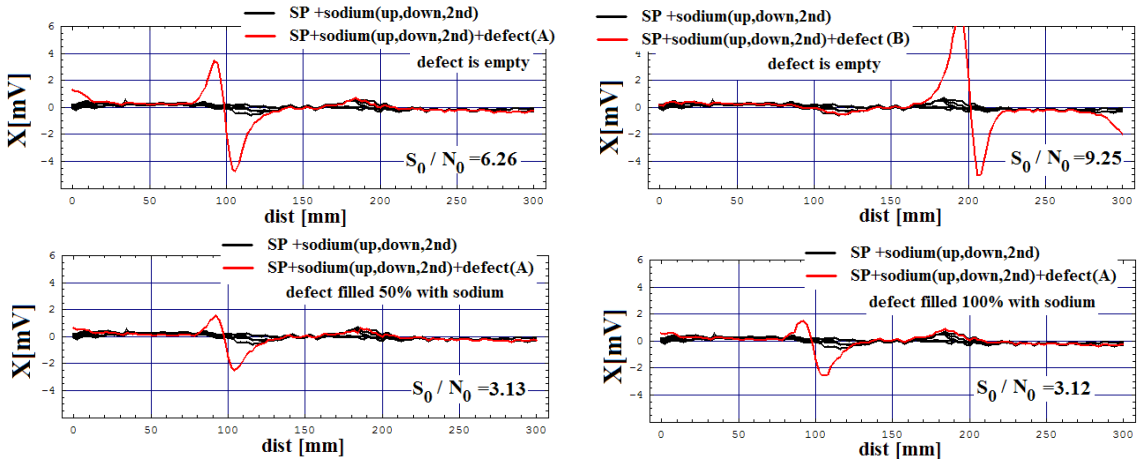

Fig. 25. Multi-frequency algorithm using parameters from case "1 tube-SP" without sodium (as shown in Table 5) for OD50%tw, position "A", "B" after removing SP and sodium signal

An improved algorithm can be obtained starting from simulations of "small SP, 1 tube with sodium" cases (parameters listed in Table 6, line 5). Fig. 26 shows the maximum noise arises starting from "sodium (down, 2nd)". The algorithm obtained for this configuration was the one which provided the best signal/noise ratio for the "small SP, 1tube with sodium" case.

When applying such algorithm to the larger model, the signal/noise ratio (Fig. 27) is similar to the one obtained for the "small SP, 1 tube no SP" case. That demonstrates that it is also possible to apply directly the algorithm generated in "small SP, 1 tube with sodium" to the data of "large SP, 9 tubes with sodium". Again, the algorithm is robust when sodium filling inside of defect increases from 50% to 100%.

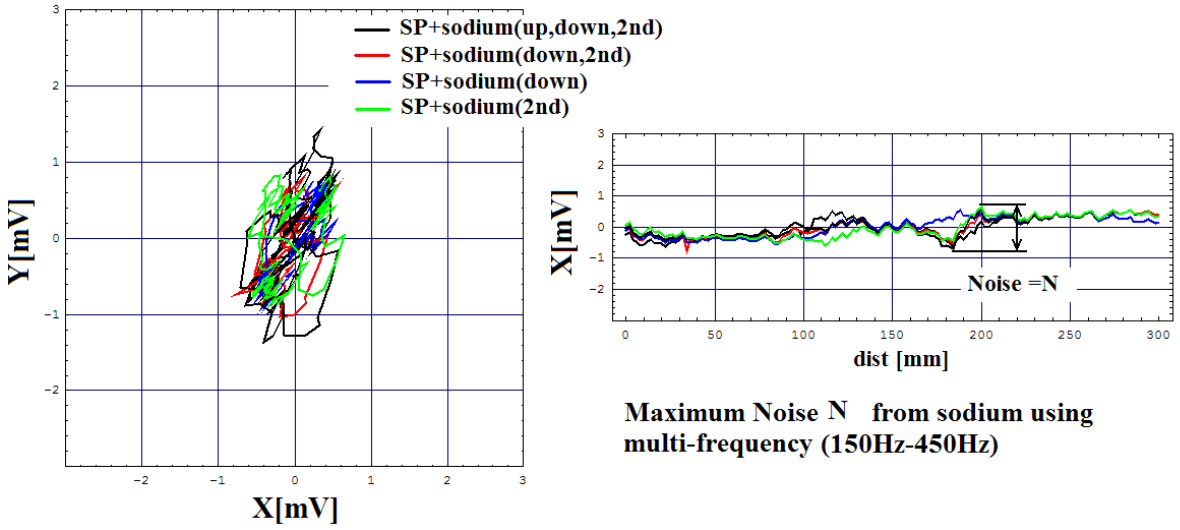

Fig. 26. Maximum noise N (1.4 mV) from sodium using multi-frequency algorithm derived from case "1 tube-SP+sodium(down, 2nd)" with sodium (as in Table 6)

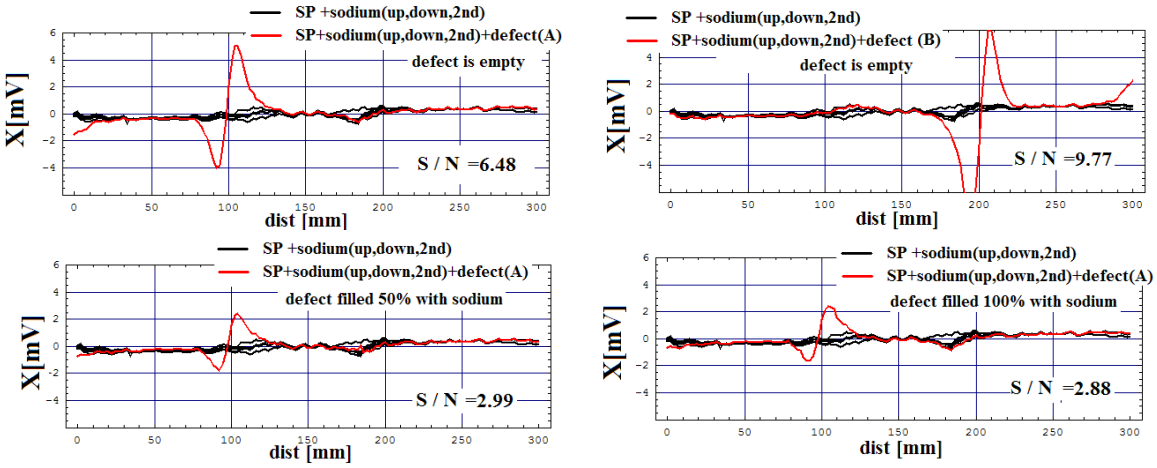

Fig. 27. Multi-frequency algorithm using parameters from case "SP+sodium(down, 2nd)" (as shown in Table 6) for OD50%tw, position "A", "B" after removing SP and sodium signal

The most optimum algorithm for the "large SP, 9 tubes with sodium" case is the one which gives the smallest noise amplitude N_0 of 0.96mV, whose parameters are listed in Table 7, line 3. The algorithm was obtained starting from the "sodium (down)" point (where we obtained k-α parameters), and maximum noise variation is plotted in Fig. 28. Application of the multi-frequency algorithm (in Fig. 29) shows the best signal/noise ratio for every case, while the signal/noise ratio of a defect filled 50% with sodium increases from 3.95 (from the "small SP, 1 tube with sodium" model) to 4.91. Also, it can be seen that further increase of filling of sodium from 50% to 100% does not worsen the performance of multi-frequency algorithm which still provide a solid 4.64 S/N ratio. Detection of the defect in "position B" under SP is achieved with even higher performance (S/N=14.2) than that of the

defect in "position A" (S/N=9.75).

The above analysis showed that even if the SP signal increases due to sodium, and decreases due to surrounding SG tubes, it is possible to obtain better signal/noise ratios. That is possible because the performance of the multi-frequency algorithm is closely related to the ratio of signals amplitude of different frequencies and uniformity of the noise distributions. In this particular case, it seems that the electromagnetic shielding due to surrounding SG tubes has a positive effect on the sodium noise distribution and its interaction with SP and tube. The increase performance in the multi-frequency algorithm is also due to the reduction in the noise level N of sodium (0.96mV) as shown in Fig. 28.

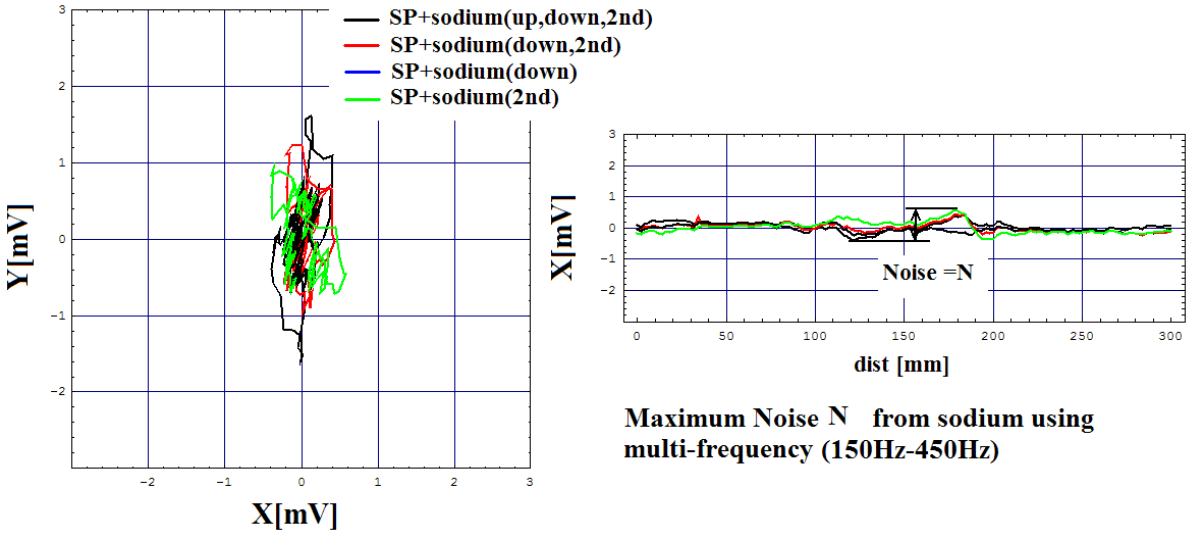

Fig. 28. Maximum noise N (0.96 mV) from sodium using multi-frequency algorithm derived from case "9 tubes-SP+sodium(down)" with sodium (as shown in Table 7)

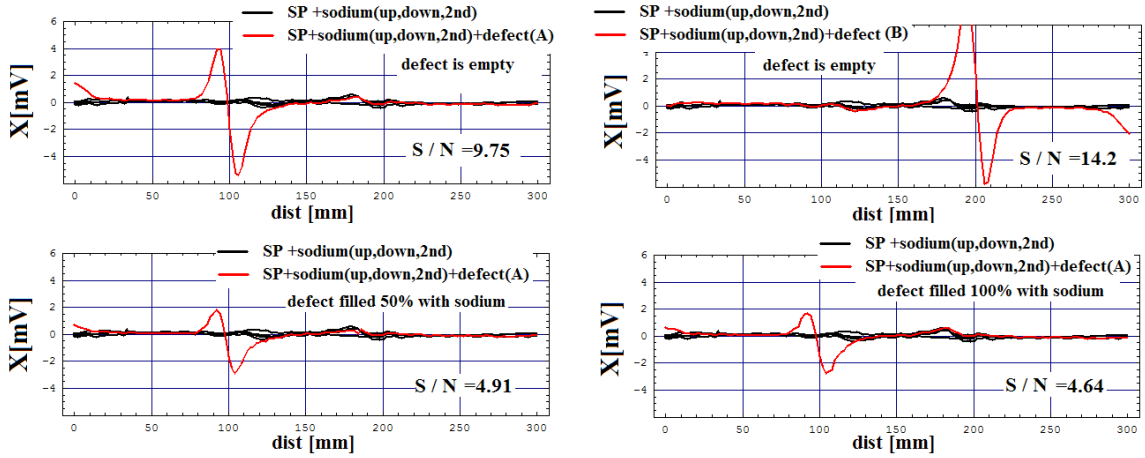

Fig. 29. Multi-frequency algorithm using parameters from case "SP+sodium(down, 2nd)" (as shown in Table 7) for OD50%tw, position "A", "B" after removing SP and sodium signal

4. Conclusion

This paper presented the numerical challenges in simulating ISI of FBR SG tubes using a 3D FEM code to analyze the electromagnetic interaction of conductive sodium with SG tubes and SP. Multi-frequency ECT, based on a linear algorithm, was applied to two models with/without sodium: one with a small SP and a single SG tube and the other one with a large SP and multiple (nine) tubes.

Simulations showed the feasibility of applying multi-frequency algorithms determined for the small model of SP with a single SG tube to the simulation data obtained from the larger model. However, the best signal/noise ratio for detecting defects under SP was obtained for multi-frequency algorithms determined from the beginning using data from the more complex and large model.

Contrary to common sense, while a 20% reduction of SP signal due to electromagnetic shielding of surrounding tubes was observed for the large model, numerical simulations showed that, despite that, it is actually possible to increase the signal/noise ratio of defects under SP of a large model with multiple SG tubes when using the appropriate multi-frequency algorithm.

References

[1] Toshihiko Yamaguchi, Ovidiu Mihalache, Masashi Ueda, Shinya Miyahara, Experimental Measurements of Eddy Current signal From SG Tubes of Fast Breeder Reactor Covered by a thin Sodium layer using a SG Mock-up, Proceedings of the 17th International Conference on Nuclear Engineering ICONE17 July 12-16, Brussels, Belgium, 2009.

[2] Sodium-NaK Enginnering Handbook, Sodium Chemistry and Physical Properties, Vol. 1, Gordon and Breach , Science Publishers, Inc., 1972.

[3] D. L. Atherton, S. Sullivan and M. Daly, A remote field eddy current tool for inspecting nuclear reactor pressure tubes, Br. J. Nondestructive Testing, 30, 1988, pp 22-28.

[4] H. Fukutomi, T. Takagi and M. Nishikawa, Remote Field eddy current technique applied to non-magnetic steam generator tubes, NDT&E International, 34, 2001, pp. 17-23.

[5] Z. Chen, M. Rebican, J. Miya and T. Takagi, Research in Nondestructive Evaluation, 16, 2005, pp. 35-53.

[6] S. Thirunavukkarasu, B. P. C. Rao, S. Mahadevan, T. Jayakumar, Baldev Raj, Zhiwei Zeng, Lalita Udpa, Satish S. Udpa, Three-Dimensional Finite Element Modeling of Remote Field Eddy Current Technique for Detection of Localized Defects, Research in Nondestructive Evaluation, Vol. 20, 2009, pp.145-158.

[7] Shuxia Tian, Zhenmao Chen, Dongli Zhang and Qiang Geng, Signal Processing Schemes for Defect Identification and Sizing from Signals of Eddy Current Testing in Nuclear Power Plant, Proceedings of the 18th International Conference on Nuclear Engineering, May 17-21, Xi'an, China, 2010.

[8] O. Mihalache, T. Yamaguchi, M. Ueda, K. Tsukimori, 3D RF-ECT Simulations of ISI of U-bend SG Tubes in FBR, Review of Progress in Quantitative Nondestructive Evaluation, Vol. 29A, American Institute of Physics, 2010, pp. 2007-2013.

[9] O. Mihalache, Advanced Remote Field Computational Analysis of Steam Generators Tubes, IOS Press, Electromagnetic Nondestructive Evaluation VII, Studies in Applied Electromagnetics and Mechanics 26, 2006, pp 220-227.

[10] Femap User Guide, Version 8.3, 2004.

[11] O. Mihalache, T. Yamaguchi, M. Ueda, S. Miyahara, 3D Remote Field Eddy Current Simulations of the Support Plates of the Magnetic Steam generator Tubes in FBR, Proceedings of the 7th NDE in Relation to Structural Integrity for Nuclear and Pressurised Components, pp. 948-956, 2009.

[12] O. Mihalache, T. Yamaguchi, M. Ueda, S. Miyahara, 3D RFEC Simulations for the In-Service Inspection of Steam Generator Tubes in Fast Breeder Reactors, International Journal of Applied Electromagnetics and Mechanics 33, 2010. pp. 1165–1171.

[13] Biro, O. and Preis, K., IEEE Transactions on Magnetics, 25, No. 4, July, 1989, pp. 3145-3159

[14] O. Mihalache, T. Yamaguchi, M. Ueda, Advancement and Performance in Large Scale Eddy Current Simulations for ISI of FBR Steam Generator Tubes", Joint International Conference on Supercomputing in Nuclear Applications and Monte Carlo 2010, Tokyo, 2010.

[15] Yamada, S., Shimizu, F., Kobayashi, K., Kaburaki, H. and Kishida, N., Performance Analysis of Parallel Mathematical Subroutine Library PARCEL, Proceedings of 4th International Conference on Supercomputing in Nuclear Applications, 2000.

[16] Ovidiu Mihalache, Shinya Miyahara, Toshihiko Yamaguchi, Takuya Yamashita, Investigations of Multi-frequency Algorithms for Detection of Defects in FBR Magnetic Steam Generators Tubes Covered with Sodium, Japan Society of Maintenology , E-Journal of Advanced Maintenance Vol.1, 2009, pp. 68-76.